



# *K*-space Algorithmic REconstruction (KAREN): a robust statistical methodology to separate Bragg and diffuse scattering

James Weng,<sup>a</sup> Eric D. Dill,<sup>a</sup> James D. Martin,<sup>a\*</sup> Ross Whitfield,<sup>b</sup> Christina Hoffmann<sup>b</sup> and Feng Ye<sup>b</sup>

Received 8 May 2019

Accepted 20 December 2019

Edited by Th. Proffen, Oak Ridge National Laboratory, USA

**Keywords:** diffuse scattering; neutron diffraction; 3D PDF analysis; plastic crystals; algorithms.

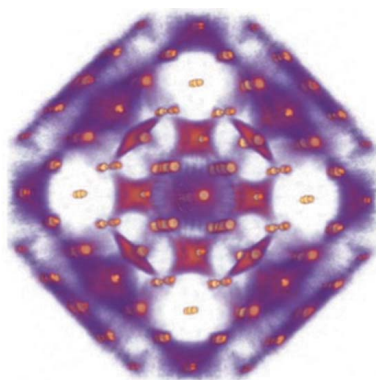
**Supporting information:** this article has supporting information at journals.iucr.org/j

<sup>a</sup>Department of Chemistry, North Carolina State University, Raleigh, NC 27695, USA, and <sup>b</sup>Neutron Sciences Directorate, Oak Ridge National Laboratory, Oak Ridge, TN 37830, USA. \*Correspondence e-mail: jim\_martin@ncsu.edu

Diffuse scattering occurring in the Bragg diffraction pattern of a long-range ordered structure represents local deviation from the governing regular lattice. However, interpreting the real-space structure from the diffraction pattern presents a significant challenge because of the dramatic difference in intensity between the Bragg and diffuse components of the total scattering function. In contrast to the sharp Bragg diffraction, the diffuse signal has generally been considered to be a weak expansive or continuous background signal. Herein, using 1D and 2D models, it is demonstrated that diffuse scattering in fact consists of a complex array of high-frequency features that must not be averaged into a low-frequency background signal. To evaluate the actual diffuse scattering effectively, an algorithm has been developed that uses robust statistics and traditional signal processing techniques to identify Bragg peaks as signal outliers which can be removed from the overall scattering data and then replaced by statistically valid fill values. This method, described as a *K*-space Algorithmic REconstruction (KAREN), can identify Bragg reflections independent of prior knowledge of a system's unit cell. KAREN does not alter any data other than that in the immediate vicinity of the Bragg reflections, and reconstructs the diffuse component surrounding the Bragg peaks without introducing discontinuities which induce Fourier ripples or artifacts from underfilling 'punched' voids. The KAREN algorithm for reconstructing diffuse scattering provides demonstrably better resolution than can be obtained from previously described punch-and-fill methods. The superior structural resolution obtained using the KAREN method is demonstrated by evaluating the complex ordered diffuse scattering observed from the neutron diffraction of a single plastic crystal of CBr<sub>4</sub> using 3D  $\Delta$ -PDF analysis.

## 1. Introduction

Diffraction of X-rays, neutrons and electrons provides a powerful tool with which to understand the structure of materials. Resolving the physical structure at the origin of a diffraction pattern, as first articulated by Laue (Friedrich *et al.*, 1913) and Bragg (1913), has enabled dramatic advances in the understanding of chemical structure and bonding. At the same time, the ordered beauty of a solved crystal structure also frequently creates a 'bias of the picture', leading to misconceptions or over-simplifications that imply the average structure solved from the Bragg diffraction of a crystal is 'the structure' of the system. The Bragg diffraction, resulting from the average long-range crystalline structure, is discrete, sharp and intense. However, surrounding the sharp Bragg diffraction, much weaker diffuse scattering is frequently also observed. It is this weak diffuse scattering that gives insight into the system's real structural, compositional, electronic and/



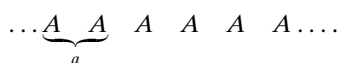
© 2020 International Union of Crystallography

or magnetic variations, which are often the key to interesting intrinsic material properties (Welberry & Weber, 2015; Weber, 2014).

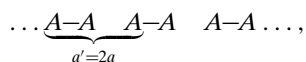
Deciphering the origin of diffuse scattering is complex. In part this is due to the fact that the distinction between Bragg and diffuse scattering is somewhat arbitrary. The diffraction pattern is the magnitude of the Fourier transform of the physical structure of a material. Bragg scattering is observed for periodic structures, and corresponds to the scattering from the long-range periodic structure. As such it is often described as a series of  $\delta$  functions, *i.e.*  $g(r^*) = \sum_{R^*} \delta(r^* - R^*)$ . Diffuse scattering is all the other scattering, the result of any deviations from the long-range periodic structure for which the measured diffraction intensity can be represented by equation (1),

$$I_{\text{total}} = I_{\text{Bragg}} + I_{\text{diffuse}} \quad (1)$$

The arbitrary distinction between Bragg and diffuse scattering can be represented by a simple 1D schematic with a regular periodic structure described as



Only Bragg diffraction will be observed for this ideal structure, consistent with the lattice constant  $a$ . If this system undergoes a Peierls distortion, for example, tending toward dimerization described schematically as



the primary scattering will still identify the original  $a$  lattice constant. However, weak scattering will be observed half way between each of the original Bragg peaks, consistent with a doubled unit cell,  $a' = 2a$ . If the distortion is small and/or not regular, the resulting interference pattern is less defined, appearing diffuse, whereas if the dimerization is more pronounced and regular, then a new long-range periodic structure is described, and what were diffuse features become defined as weak Bragg peaks.

There are a vast number of possible perturbations to an average structure, resulting in a much more complex diffuse structure, and thus many real systems exhibit a much less clear distinction between what is diffuse and what is Bragg scattering. Nevertheless, deviations from the ideal structure are often critical features with respect to defining the properties of a material (Egami & Billinge, 2012). Thus, there is a strong desire to understand the real structural perturbations that give rise to diffuse scattering patterns.

In conventional usage, deviations from the regular periodic structure that give rise to the diffuse scattering have been described as ‘local structure’, which is contrasted with the ‘average structure’. The concept of ‘local structure’ has become particularly prevalent in descriptions of pair distribution function (PDF) analysis of total scattering (Egami & Billinge, 2012). While the short-range pair correlations observed in a PDF describe the local structure, it is equally important to recognize that they too are representations of the

average structure. Herein, local variation from the long-range periodic structure causes diffuse scattering, but all diffraction, both Bragg and diffuse, is a result of the interference pattern created by waves diffracted by the ensemble of particles making up the entire sample. The averaging inherent in a diffraction experiment is also a fundamental property of the Fourier transform and arises as a consequence of the projection-slice theorem (Bracewell, 1990). Thus, it is important to clarify that all diffraction represents average structure, *i.e.* Bragg scattering represents average long-range periodic structure, and diffuse scattering represents average perturbation from this long-range periodic structure.

Because diffuse scattering is generally three to six orders of magnitude less intense than Bragg scattering, physical measurement further complicates its study. This is particularly detrimental when diffuse features are in the immediate vicinity of strong Bragg peaks. Diffuse scattering was observed in early diffraction studies using film techniques, which captured spatial resolution of diffuse scattering reasonably effectively, but the dynamic range of the film significantly limited quantification (Welberry & Weber, 2015; Weber, 2014). Subsequent diffractometers equipped with single-point scintillation detectors, while excellent for quantification of the intensity of the diffracted signal, are not well suited to comprehensive mapping of reciprocal space because of their small spatial coverage. More recent developments of area detectors, such as image plates, CCDs and CMOS detectors used on in-house X-ray laboratory and synchrotron sources, improve the ability to both spatially map and quantify the intensity of diffuse scattering, although artifacts due to pixel saturation or pixel-to-pixel bleeding are frequently introduced (Goossens *et al.*, 2005). The hybrid photon-counting PILATUS detectors, with a substantially greater dynamic range, appear to reduce some of the artifacts for synchrotron measurements (Weber *et al.*, 2008). We find the continuous readout counting afforded with neutron scattering using an array of time-of-flight detectors on the CORELLI and TOPAZ diffraction instruments at the Spallation Neutron Source (SNS), Oak Ridge National Laboratory, is less likely to saturate and thus reduces the number of artifacts created by intensity bleeding into neighboring pixels.

However, even with careful measurement of both Bragg and diffuse scattering, the Bragg diffraction dominates the real-space structural interpretation due to the significant intensity differential. After the transformation from reciprocal to real space through a Fourier transform, strong features, like Bragg peaks, continue to dominate the transformed pattern while the signal of interest remains insignificant. Thus, there is value in developing methods to separate Bragg and diffuse scattering to afford their independent analysis.

A punch-and-fill method has been employed to separate Bragg and diffuse scattering (Kobas *et al.*, 2005*a,b*). This method requires prior knowledge of the material’s unit cell such that the Bragg reflections can be subtracted from, or ‘punched out’ of, the total diffraction pattern according to the known lattice spacing with an arbitrary punch diameter,  $w(r^*)$ , selected to remove the strongest Bragg reflections completely.

Application of this punch-and-fill strategy has included Patterson analysis of only the punched diffraction pattern, or evaluation of diffraction patterns for which various interpolated functions fill the punched holes (Weber & Simonov, 2012; Sangiorgio *et al.*, 2018; Roth & Iversen, 2019; Krogstad *et al.*, 2019). It has been stated that ‘...punching the Bragg reflections mainly removes the high-frequency part of scattering intensity. The low-frequency part, which mostly corresponds to the overall distribution of diffuse scattering, is hardly affected by this procedure.’ (Kobas *et al.*, **2005a OR 2005b?**). The latter assumption that the diffuse scattering is primarily represented by the low-frequency part of the scattering is the basis used to justify a low-frequency fill function. However, both the punch-only and punch-and-fill strategies introduce artifacts and/or bias into the interpretation of the chemical or physical origin of the diffuse scattering.

Patterson and PDF analyses of diffraction data rely on the Fourier transformation of the scattering function, therefore sharp discontinuities created by punching out the Bragg reflections generate severe ripple artifacts in the real-space data. Such ripples are a consequence of the Gibbs phenomenon, a behavior of any eigenfunction series at a jump discontinuity (Eric W. Weisstein, *Gibbs Phenomenon*, from *MathWorld – A Wolfram Web Resource*, <http://mathworld.wolfram.com/GibbsPhenomenon.html>, accessed March 2019). To minimize the Fourier ripple, or Gibbs artifacts, the holes may be filled before Fourier transformation. Only filling with a smooth function will prevent the introduction of Fourier ripples.

Because of the presumption that ‘diffuse scattering is by far broader than the Bragg profiles, ... interpolation of the diffuse beneath the Bragg scattering [is suggested to] provide a reasonable approximation to the real diffuse intensities.’ (Weber & Simonov, 2012). Thus, one strategy to fill the punched scattering pattern is to apply a Gaussian convolution to the punched data to interpolate missing data (*MANTID* punch-and-fill; Arnold *et al.*, 2014). Alternative strategies interpolate only the punched region with an isotropic Gaussian (Krogstad *et al.*, 2019). However, as will be demonstrated below, diffuse scattering is not necessarily a smooth continuous isotropic function.

We find that there is a need for an alternative strategy to separate Bragg from diffuse scattering that: (i) does not introduce discontinuities which produce Fourier ripples, (ii) does not introduce bias as to the nature of the diffuse scattering, (iii) is not dependent on a fixed arbitrary window to remove Bragg scattering, and (iv) does not require prior knowledge of the material’s unit cell in order to determine the Bragg intensity that should be subtracted. To accomplish this, we have consulted signal-processing literature (Pearson *et al.*, 2016) to develop a novel strategy, *KAREN* (*K-space Algorithmic REconstruction*), whereby Bragg peaks are identified as signal outliers. Once Bragg peak locations are determined, the peaks are removed and the removed regions are reconstructed to match the underlying diffuse scattering. Importantly, we will show that *KAREN* does not modify or alter any non-outlier data and thus introduces the minimum possible

bias into the measured data. In addition, robust statistical estimators used for outlier detection are insensitive to measurement-related noise, making them well suited for handling difficult-to-measure signals.

## 2. What is the signal to be measured?

Before describing the details of our algorithm to separate Bragg and diffuse scattering, it is useful to consider the expected manifestation of diffuse scattering. A majority of reports describing diffuse scattering suggest it to be ‘broad’, ‘continuous’, ‘streak-like’ *etc.* With respect to the evaluation of crystalline systems, the ‘broad continuous’ presumption is reinforced by the modest-to-low pixel resolution of detectors,

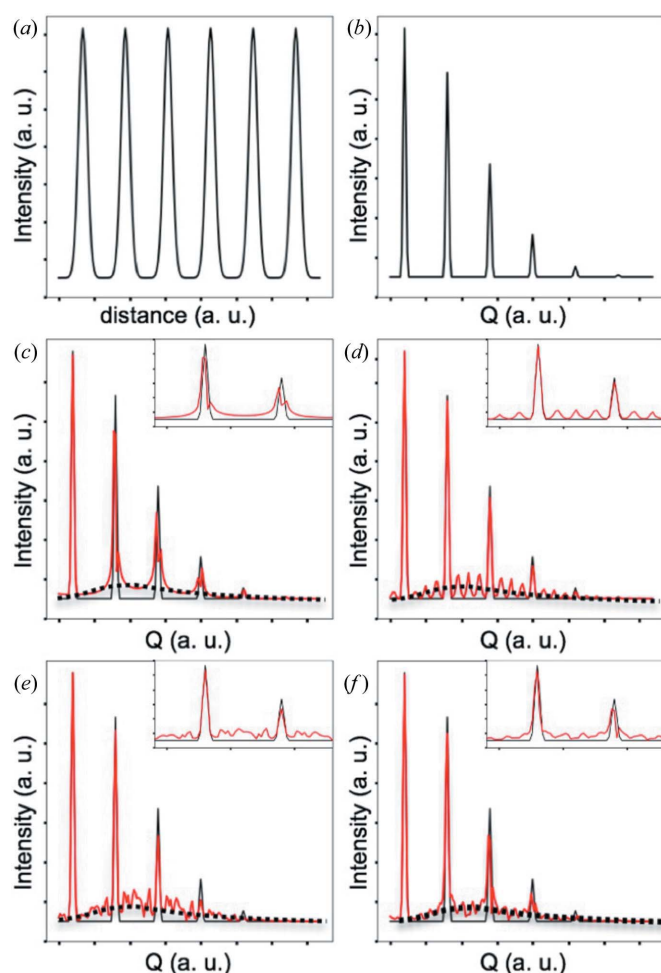


**Figure 1**  
 (a) A hypothetical 1D crystal of Gaussians with FWHM = 7.5 units and separated by 30 units. (b) The diffraction pattern of the ideal 1D crystal. (c)–(f) Diffraction patterns of perturbed 1D crystals (red) superimposed on the diffraction of the ideal average lattice (black) with (c) the first half of Gaussians shifted to the left by 3 units and the second half shifted to the right by 3 units; (d) every other Gaussian randomly shifted left or right by up to 3 units; (e) each Gaussian randomly shifted left or right by up to 3 units; and (f) the first half of the Gaussians shifted to the left randomly by up to 3 units and the second half of the Gaussians shifted to the right randomly by up to 3 units. Insets present the second and third peaks on an expanded  $Q$  scale, which more clearly demonstrates the peak splitting observed in panels (c) and (f). The dotted black lines are the same smoothed diffuse function overlaid on each pattern.

by experimental methods that continuously rotate the crystal during measurement and/or by evaluation of polycrystalline powders. ‘Jitter’ or speckling in the data is frequently assumed to be noise, for which application of a low-pass filter (Goossens *et al.*, 2005) or smoothing polynomial (Juhás *et al.*, 2013) is frequently applied. Notably, however, the calculated inverse Fourier transform of physical images only becomes broad and continuous for isolated objects. As is clearly visible in the various 2D optical transforms shown in the *Atlas of Optical Transforms* (Harburn *et al.*, 1975), the Fourier transforms of ensembles become increasingly speckled with the increasing number of components in the physical image.

Consider, for example, the diffraction from the long-range ordered pattern of Gaussians with a FWHM of 7.5 units and separated by 30 units shown in Fig. 1(a). The Fourier transform of that ideal 1D ‘crystal’, the Bragg diffraction, is given in Fig. 1(b). Keeping the average structure constant but inserting a grain boundary for which the first half of the Gaussians are shifted by three units to the left and the second half of the peaks are shifted by three units to the right, the diffraction pattern of Fig. 1(c) is calculated. Here, each of the previous Bragg peaks is split, and the base of each Bragg peak is significantly broadened by an apparent diffuse background. Alternatively, again with a constant average structure, let every other Gaussian be randomly shifted left or right by up to three units. The corresponding diffraction pattern is given in Fig. 1(d). The diffraction pattern for the 1D crystal with each Gaussian randomly shifted left or right by up to three units is given in Fig. 1(e), and that for the random distortion with a grain boundary (*i.e.* the first half of the Gaussians shifted by a random amount up to three units to the left and the second half of the Gaussians shifted by a random amount up to three units to the right) is shown in Fig. 1(f).

Consistent with the common average periodic structure of each of these models, there is very little variation in the Bragg scattering between that of the ideal crystal and the distorted crystals. It is further important to recognize that the average diffuse scattering, represented by the smoothed dotted lines in Figs. 1(c)–1(f), is essentially equivalent for each of the perturbed model structures. Importantly, the jitter in these calculated data is not noise. It is a direct result of the specific perturbations, and thus provides critical data that must be preserved to obtain an accurate analysis of the diffuse scattering in order to understand the local perturbations.

The complexity of the diffraction patterns increases, and thus the separation of diffuse from Bragg scattering becomes more complicated, for higher-dimensional systems. Consider the area described by Figs. 2(a) and 2(b) for which each has an equivalent number of filled pixels. In Fig. 2(a) the filled pixels are randomly distributed on 10.5% of the odd values on a square spiral emanating from the center. In Fig. 2(b) the same number of pixels are filled in the pattern of an Ulam spiral, *i.e.* a square spiral emanating from the center of the area for which each pixel corresponding to a prime number is filled. The calculated diffraction patterns for each image are given as Figs. 2(c) and 2(d), respectively. Both exhibit the same Bragg scattering, but their patterns of diffuse scattering are distinct,

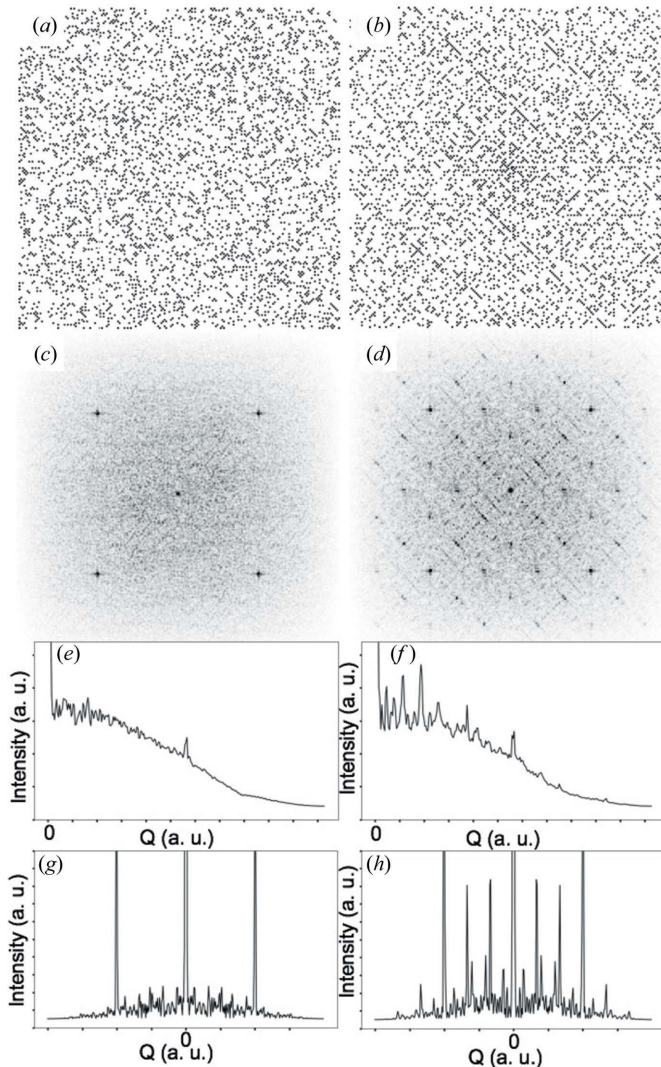


**Figure 2** (a) Pixels randomly distributed on 10.5% of the odd values of a square spiral. (b) Pixels distributed along an Ulam spiral. (c) and (d) 2D diffraction patterns, and (e) and (f) 1D radially integrated patterns, calculated for the pixel distributions in panels (a) and (b), respectively. (g) and (h) Diagonal cross sections of the diffraction images in panels (c) and (d), respectively. Panels (e)–(g) are plotted on an expanded intensity scale to accentuate the diffuse scattering. Full-scale plots of panels (g) and (h) are given in Fig. S1

with the Ulam spiral model exhibiting notably ordered patterns of diffuse scattering. The diffuse scattering is more than 50 times less intense than the Bragg scattering, as seen in the supporting information (Fig. S1).

Radially integrating each of these images [Figs. 2(e) and 2(f), respectively, equivalent to 1D powder diffraction patterns] exhibits a more Bragg-like structure for the Ulam spiral, but the underlying diffuse scattering from both models is nearly equivalent, and reasonably presumed to be a broad continuous function. By contrast, evaluating the diagonal cross section through each of these images [Figs. 2(g) and 2(h), respectively], like the images of Figs. 2(c) and 2(d), clearly demonstrates that the details of the perturbation from the average structure are found in the jitters of the diffuse scattering.

Notably, no simple punch function can effectively remove the Bragg scattering from the diffuse in these patterns. Furthermore, applying a Gaussian convolution, like collapsing the higher-order diffraction data into a 1D powder pattern, averages the diffuse scattering such that it would not be possible to distinguish the distinct structural perturbations.

Thus, to best analyze diffuse scattering, it is necessary to obtain high-resolution 3D scattering data from single-crystalline samples. Furthermore, to analyze such diffuse data, it is necessary to remove the Bragg scattering without manipulation of the underlying diffuse scattering.

### 3. KAREN (K-space Algorithmic REconstruction)

KAREN is a single-stage nonlinear digital filter which is based on the Hampel filter (Pearson *et al.*, 2016). The Hampel filter is a decision filter that operates on the central value in the data window by replacing outliers with the median of all values in the window. An implementation of KAREN was recently integrated into the MANTID software suite (Arnold *et al.*, 2014).

The total scattering intensity,  $I_{\text{total}}$ , is described as the sum of the  $I_{\text{Bragg}}$  and  $I_{\text{diffuse}}$  components [equation (1)]. Because Bragg peaks are significantly more intense than the diffuse scattering components, the total scattering intensity may be considered to be some function with arbitrarily positioned outliers, *i.e.* the Bragg peaks.

With KAREN, the voxels of the reciprocal-space volume corresponding to the 3D diffraction intensity are evaluated for outliers. Using Hampel filter methods, the voxel in the center of a moving window is determined to be an outlier if its intensity exceeds three standard deviations ( $3\sigma$ ) of the intensity of the other voxels contained within the window. In KAREN, an  $N \times N \times N$  cubic moving window is employed, with  $N$  selected to be the width of the primary diffuse scattering features.

The value for  $\sigma$  is estimated from the median absolute deviation, MAD, by equation (2),

$$\sigma \simeq 1.4826 \times \text{MAD}. \quad (2)$$

The value 1.4826 is a scaling factor derived from the assumption that the data within the window are normally distributed (Rousseeuw & Croux, 1993). The MAD for some set of values  $X$  is defined by equation (3),

$$\text{MAD} = \text{median} [ |X_i - \text{median}(X)| ]. \quad (3)$$

The MAD [equation (3)] and the MAD estimate of  $\sigma$  [equation (2)] are robust statistics for which the inclusion of outliers does not significantly change their values. This is in contrast to common calculations of the standard deviation [*i.e.*  $\sigma = [\sum_{i=1}^n (x_i - \bar{x})^2 / (n-1)]^{1/2}$ ], which can be significantly shifted by the inclusion of even a single corrupted value. Testing with randomly generated normally distributed data indicates that roughly 20% of a data set may consist of outliers before the values returned for the MAD, or  $\sigma$  from equation (2), are significantly altered.

Voxels identified as outliers are determined to be the Bragg scattering, as distinct from the diffuse scattering. The diffuse scattering intensity underneath the Bragg scattering voxel is assumed to be statistically insignificant with respect to the Bragg scattering intensity. The compilation of all outlier voxels is defined as  $I_{\text{Bragg}}$ . Before analysis such as  $\beta$ -PDF (*i.e.* PDF analysis of only the Bragg diffraction), the Bragg peaks should ideally be fitted by a Voigt function, for example, so as not to introduce termination artifacts into the Fourier analysis. Importantly, by defining Bragg scattering as the outliers of the total scattering function, no prior knowledge of the material's unit cell is required. As such, the above-noted arbitrary distinction between the Bragg and diffuse scattering of a Peierls distorted system is moot, being determined only by the user-defined statistical threshold for outlier identification. This method for Bragg peak identification may be particularly advantageous for the evaluation of modulated crystalline structures, as it allows separation of scattering induced by structural modulation from scattering created by other disordering effects.

By contrast, the diffuse scattering component of the outlier voxels is significant with respect to identification of the overall diffuse scattering. Thus, to obtain the complete  $I_{\text{diffuse}}$  it is necessary to reconstruct the diffuse scattering component of the outlier voxels. Because analysis of the diffuse scattering frequently relies on Fourier techniques, it is critical that the reconstruction method does not introduce sharp discontinuities between the non-outlier voxels and the reconstructed voxels.

While various fitting routines can be used to reconstruct the void remaining after outlier subtraction, computational efficiency must also be considered, given the total number of voxels that must be evaluated in a given diffraction pattern. Were computational time not a factor, reconstruction of the void resulting from removal of  $I_{\text{Bragg}}$  could effectively be accomplished by using solutions of the heat equation or biharmonic equation, for example, as is commonly employed for image reconstruction (Schönlieb, 2012). Alternatively, the void can be reconstructed by convolution with a Gaussian kernel (Krogstad *et al.*, 2019). However, these methods increase the computational time by about three orders of magnitude, thus demanding a more computationally efficient approximation.

It is reasonable to assume that the actual  $I_{\text{diffuse}}$  underneath the Bragg peak should be between a maximum of the (median +  $3\sigma$ ) of all voxels in the defined window and a minimum of the median of all voxels in the window. In the window, the maximum of (median +  $3\sigma$ ) is the threshold used to distinguish Bragg and diffuse scattering. A minimum of the median is assumed, since to suggest otherwise would consider the diffuse scattering under the Bragg scattering to be lower in intensity than the surrounding diffuse scattering. Applying these approximations to actual data for the perovskite PMN [ $\text{Pb}(\text{Mg}_{1/3}\text{Nb}_{2/3})\text{O}_3$ ], collected on the CORELLI instrument at the SNS (Krogstad *et al.*, 2018) (Fig. 3), it is observed that reconstruction of the outlier-subtracted voids with the (median +  $3\sigma$ ) is likely to over-estimate the diffuse component

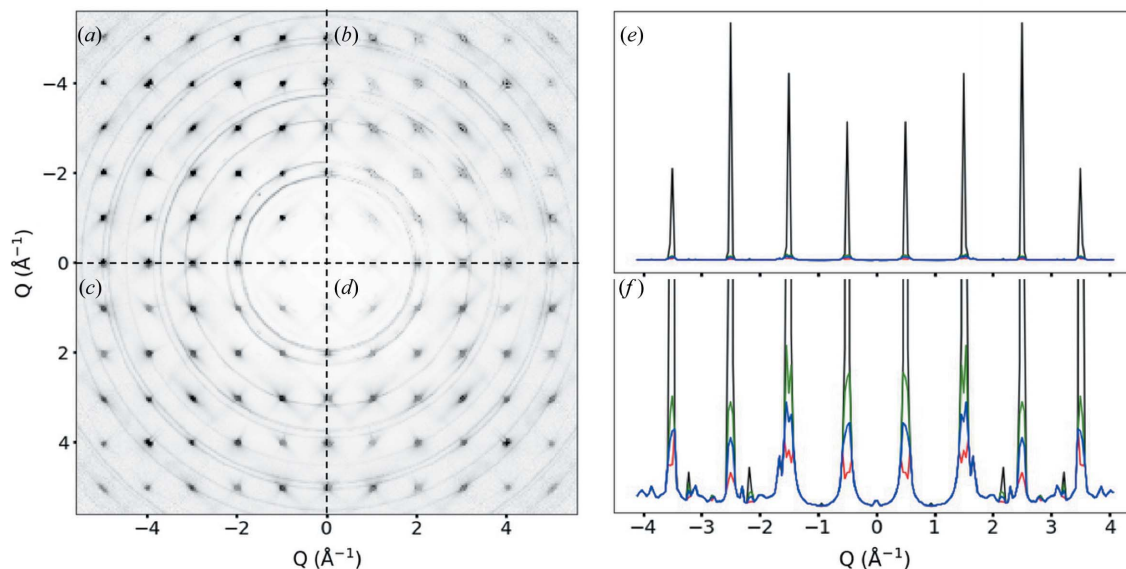


**Figure 3**  $(100)^*$  cross section of the reciprocal-space volume of the neutron diffraction of PMN, collected on CORELLI (elastic only; Ye *et al.*, 2018). The powder rings correspond to the diffraction from the Al sample canister. (a) Total scattering, *i.e.* Bragg + diffuse. Bragg scattering outliers are removed and replaced with (b) the median value of the window, (c) the median +  $3\sigma$ , the threshold for outlier detection, and (d) the median + 2.2 MAD. (e) A 1D plot along the  $[100]^*$  vector, with the total scattering represented as a black line, the median reconstruction (red), the median +  $3\sigma$  (green) and median + 2.2 MAD (blue). (f) The data from panel (e) replotted on an expanded y scale.

underneath the Bragg peak [Figs. 3(c) and 3(e)], whereas reconstruction with only the median of the Hampel window under-represents the diffuse scattering intensity and results in significantly distorted peak shapes [Figs. 3(b) and 3(e)]. The value of the median, like the standard deviation, is sensitive to outliers, though less so than the latter. In particular, when, as is observed for the diffuse scattering of PMN, the diffuse scattering is localized into anisotropic and reasonably sharp star or cross-like patterns for which there is no diffuse intensity in much of the 3D window, reconstruction by replacement with the median leads to speckle artifacts where portions of the reconstructed intensity are lower than the surrounding region. By contrast, addition of the MAD to the median significantly attenuates outlier and anisotropic effects. Evaluating a variety of simulated and actual diffraction patterns, empirically we find that reconstruction by replacing outlier voxels with the (median + 2.2 MAD) reasonably reconstructs the diffuse scattering with minimal distortion [Figs. 3(d) and 3(e)]. This value of the (median + 2.2 MAD) is approximately the (median +  $1.5\sigma$ ). Notably, Fourier transform of the diffuse scattering data exhibits no substantive difference between reconstructions based on the more computationally intensive use of solutions to a differential equation such as the heat equation, or those based on the simple (median + 2.2 MAD) approximation. Furthermore, it is important to recognize that reconstruction leaving too much Bragg intensity in the diffuse function has a minimal effect on subsequent PDF analysis, since it contributes to existing positive pair correlations. By contrast, as will be demonstrated below, deficient reconstruction of the diffuse scattering creates novel features in the diffuse structure factor which introduce artifacts in the PDF corresponding to physically impossible correlations.

#### 4. KAREN versus punch-and-fill

The diffuse scattering corresponding to the plastic crystalline phase of  $\text{CBr}_4$  provides an excellent proving ground with which to compare and contrast *KAREN* and prior methods used to separate the Bragg and diffuse scattering. Plastic crystals of  $\text{CBr}_4$  are soft and easily deformable. The plastic crystalline phase exhibits a high overall symmetry, but is also characterized by a high degree of orientational and displacive disorder. Details of the structural disorder remain a subject of some debate (Folmer *et al.*, 2008; Temleitner & Pusztai, 2010). Due to the structural disorder, the diffuse scattering contribution is very significant compared with the Bragg scattering and is therefore a good example to study in this context.

Neutron diffraction data of  $\text{CBr}_4$  were collected and analyzed. Specifically, the data were analyzed with *KAREN*, the punch-only and the punch-and-fill methods (Weber *et al.*, 2008; Kobas *et al.*, **2005a OR 2005b?**; Weber & Simonov, 2012; Krogstad *et al.*, 2019).

A sample of  $\text{CBr}_4$ , sufficient to form a 2 cm long ingot in a 2 mm diameter Kapton tube, was mounted on the TOPAZ beamline (Spallation Neutron Source, Oak Ridge National Laboratory). Analogous to previous work (Folmer *et al.*, 2008; Dill, 2013), a single plastic crystal was grown *in situ* by heating the sample under a stream of argon using an Oxford Cryostream up to the melting point (383 K), then quenching *in situ* at  $6 \text{ K min}^{-1}$  to a crystal growth isotherm  $T_{\text{iso}} = 355 \text{ K}$ . Cross sections of the collected reciprocal space,  $(111)^*$  and  $(100)^*$ , and a full 3D rendering are given in Fig. 4. (A movie of the 3D reciprocal space is provided as supporting information.) The presence of relatively intense anisotropic sheets and volumes of diffuse scattering provide a challenging test data set for the

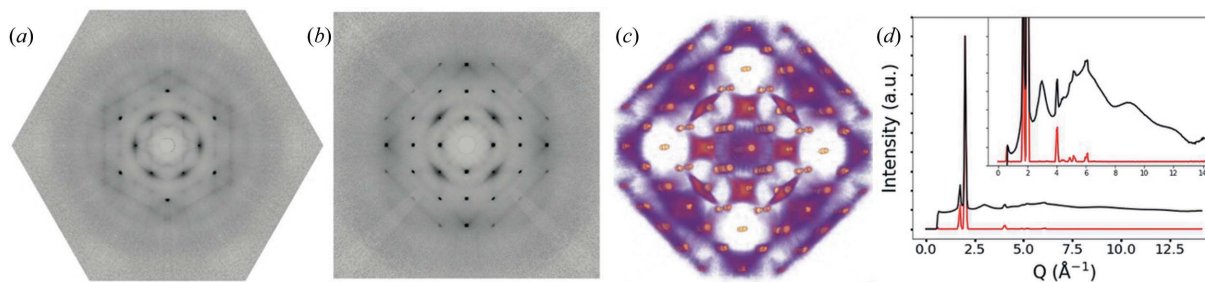


Figure 4

Total neutron scattering of plastic crystalline  $\text{CBr}_4$ . (a) The  $(111)^*$  cross section. (b) The  $(200)^*$  cross section. (c) A 3D rendering, looking just off the  $[100]^*$  axis. (d) A 1D diffraction pattern, corresponding to integration over the full reciprocal-space volume (black) and the independent integration of the Bragg scattering (red). The inset shows an expanded intensity scale.

separation of Bragg and diffuse scattering. Notably, all the anisotropic structure information of the diffuse scattering is lost if the diffraction volume is integrated and collapsed to 1D, or if a polycrystalline sample were evaluated as is typical for a majority of PDF analyses. Furthermore, while in the 3D volume the Bragg diffraction features are clearly outliers, when integrated to 1D it would be extremely difficult to extract Bragg and diffuse components [Fig. 4(d)], particularly for the weaker Bragg reflections between  $4$  and  $6 \text{ \AA}^{-1}$ .

Multiple methods to separate the diffuse scattering component from the total 3D scattering data were applied, for which  $(100)^*$  cross sections are shown in Fig. 5 and Fig. S2. The original data are given in Fig. 5(a). The data were evaluated using the full *KAREN* algorithm, whereby the outlier voxels are replaced by the (median + 2.2 MAD) [Fig. 5(b)], and with a modified *KAREN* algorithm, whereby the outlier voxels are replaced by the median of the surrounding region (not shown).

Previous punch methods require prior knowledge of the unit cell, such that an isotropic hole of defined radius can be punched in the structure factor data at calculated reciprocal-lattice positions to remove the Bragg components (Kobas *et al.*, 2005a OR 2005b?). In Fig. S2(c) lattice-determined Bragg reflections are removed with an 8-pixel spherical punch. Notably, this method imposes the same fixed punch on regions of reciprocal space where no Bragg intensity is measured, which will be shown to create artifacts in the PDF. We also evaluated a variable-punch method in which only the *KAREN*-identified outliers are removed [Fig. S2(e)], by which any anisotropy, variable size and absences of the Bragg reflections are accounted for.

The initial punch-and-fill implementation (Kobas *et al.*, 2005a,b) as implemented in the *MANTID* software suite (*MANTID* punch-and-fill) applies a Gaussian convolution over the whole scattering pattern to fill the punched voids [Fig. S2(d)]. Here the type of Gaussian convolution can significantly impact the interpolated fill. When implemented with a simple Gaussian convolution, such as found in the *SciPy* signal library (<https://docs.scipy.org/doc/scipy/reference/signal.html>), even relatively large Gaussian kernels do not completely fill the punched voids. By contrast, the *Astropy* convolution library (Price-Whelan *et al.*, 2018) introduces a method to replace missing data during convolution such that incomplete

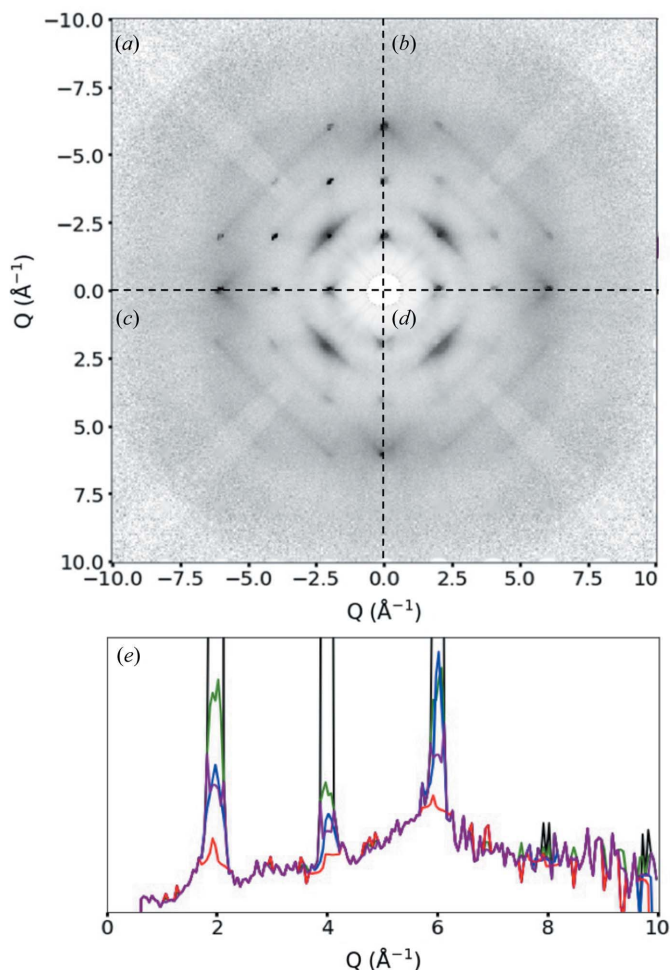


Figure 5

The  $(100)^*$  cross section of the diffuse scattering of  $\text{CBr}_4$ . (a) Original data. (b) *KAREN* reconstructed diffuse scattering. (c) Bragg scattering removed with a fixed 8-pixel punch filled by convolution with a Gaussian kernel and (d) with a fixed 12-pixel punch filled by convolution with a Gaussian kernel. (e) A 1D plot along the  $[100]^*$  vector of the unmodified total scattering (black), the *KAREN* reconstructed diffuse scattering (green), the *KAREN* reconstructed diffuse scattering with a median-only fill (purple), the 8-pixel punch and HC-fill reconstructed diffuse scattering (blue), and the 12-pixel punch and HC-fill reconstructed diffuse scattering (red). Gaussian kernels with  $\sigma = 1$  were used for interpolation.

filling effects are minimized. With the *Astropy* convolution method, the punched voids are completely filled, but the magnitude of the interpolated residual diffuse scattering under the punched Bragg peak is significantly dependent on the size of the punched void. The *MANTID* punch-and-fill implementation uses the *Astropy* convolution library, and hereafter in this article will be referred to as the whole-pattern convolution fill, WPC-fill.

The punch-and-fill method described by Krogstad *et al.* (2019) also fills the voids using the *Astropy* convolution library (Price-Whelan *et al.*, 2018), but only utilizes the convoluted values from the punched regions, leaving the remainder of the data unmodified. Hereafter this method will be referred to as the hole-convolution fill (HC-fill) method. In this article, the punch–HC-fill method is implemented using 8-pixel and 12-pixel spherical punches and a Gaussian kernel of  $\sigma = 1$ , with data shown in Figs. 5(c) and 5(d), respectively. For this data set, the use of either a smaller punch diameter (6 pixels) with the same  $\sigma = 1$  Gaussian kernel, or a larger  $\sigma = 2$  Gaussian kernel with a punch diameter of either 6 or 8 pixels, creates ringing artifacts which appear as a checkerboard pattern in the calculated PDF, making the data uninterpretable (Fig. S3).

As highlighted by the 1D [100]\* cuts through these images [Fig. 5(e) and Fig. S2(g)], the punch-only, *KAREN* and punch–HC-fill implementations leave the majority of the measured diffraction pattern intact. By contrast, while removing the discontinuities of the punch, the WPC-fill also removes all of the jitter from the pattern, imposing an isotropic character on the pattern. Notably, the various methods reconstruct different amounts of diffuse scattering underneath the punched Bragg reflections. As apparent from Fig. 5(e), the reconstructed diffuse scattering obtained by the HC-fill method is substantially dependent on the size of the punched

holes. Furthermore, both the HC-fill and WPC-fill methods reconstruct the diffuse scattering under the Bragg peaks to a value that is comparable to the *KAREN* algorithm only when a median fill is applied [Figs. 3(f) and 5(e)].

The effectiveness of each of these methods to extract the unique diffuse scattering is most apparent upon evaluation of the  $\Delta$ -PDF, the PDF calculated from only the diffuse component of the scattering (Weber & Simonov, 2012). The  $\beta$ -PDF, calculated from only the Bragg scattering and indicative of the fully ordered part of the structure, is not particularly sensitive to the separation and reconstruction methods used. It is useful to consider the positive and negative contributions of the  $\Delta$ -PDF independently. Real vectors between the same elements contribute to positive correlations and real vectors between different elements contribute to negative correlations.

Movies of a full rotation of the 3D  $\Delta$ -PDF of plastic crystalline  $\text{CBr}_4$  showing negative correlations for a 9.4 Å cubic real-space volume, calculated from the *KAREN*, fixed and variable punch-only methods, and the punch–HC-fill method reconstructions, are given as supporting information. Select (100) cross sections showing both positive and negative correlations, calculated to 30 Å, are shown in Fig. 6 and Fig. S4. Because the *KAREN* [Fig. 6(a)], punch-only [Figs. S4(b) and S4(c)] and punch–HC-fill [Figs. 6(b) and 6(c)] strategies do not alter any of the data outside of the punched regions, *i.e.* retaining all of the measured jitter in the diffuse scattering as well as the low-frequency components, the short-range structures revealed by these methods are extremely similar.

Details of the structure of the plastic crystalline phase of  $\text{CBr}_4$  will be discussed in a subsequent paper. Nevertheless, here we note that each of the methods that do not alter the diffuse scattering outside of the punched regions clearly

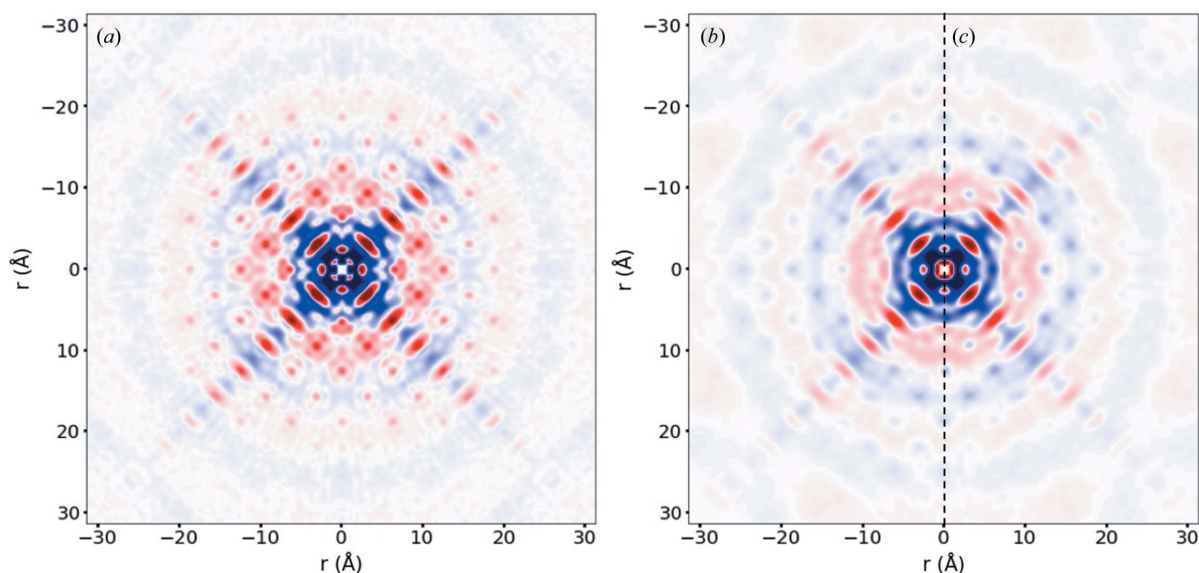


**Figure 6** The (100) cross section of the  $\Delta$ -PDF of plastic crystalline  $\text{CBr}_4$  calculated to  $r = 30$  Å from neutron scattering data after removal of the Bragg scattering and reconstruction of the diffuse scattering using (a) the *KAREN* algorithm, (b) the punch–HC-fill method with an 8-pixel diameter punch and interpolation by a  $\sigma = 1$  Gaussian kernel and (c) the punch–HC-fill method with a 12-pixel diameter punch and interpolation by a  $\sigma = 1$  Gaussian kernel. Intensity is plotted on a log scale, with positive correlations red and negative correlations blue. In these renderings, the origin of the  $\Delta$ -PDF has been set to zero.

resolve the paired dodecahedron in the center of the negative  $\Delta$ -PDF corresponding to the paired six possible positions of the C—Br vectors (*i.e.* oriented along the [110] directions, but split due to the  $109^\circ$  Br—C—Br bond angle) (Folmer *et al.* 2008; Dill, 2013). As clearly seen in the cross-section plots of Fig. 6, the cross-like extended order along the [110] directions is also consistent with earlier literature suggesting that the C—Br bonds tend to be localized along the [110] directions of the unit cell (Folmer *et al.* 2008; Dill, 2013; Coulon & Descamps, 1980; More *et al.*, 1980).

Notably, while the core nearest-neighbor structure is not significantly different from any of the punch-and-fill methods, the higher  $r$  features are significantly dependent on the method of fill. The WPC-fill reveals very little higher  $r$  structure, although this loss of structural detail is less significant for the variable  $r$  punch afforded by filling only the outlier holes identified by the *KAREN* method [Figs. S4(*b*) and S4(*d*)].

Consistent with the residual Bragg intensity that remains with the *KAREN* extraction of the diffuse scattering, positive correlations are observed in the  $\Delta$ -PDF on the lattice sites. More importantly with respect to the structural origins of the diffuse scattering, the  $\Delta$ -PDF surrounding each of these lattice sites also reveals a pattern of correlations consistent with the dodecahedron resulting from the various C—Br orientations. By contrast, the  $\Delta$ -PDF of the diffuse scattering from the punch—HC-fill methods introduces novel negative correlations at lattice sites [Figs. 6(*b*) and 6(*c*)]. These negative structure correlations are more sharply manifest for the largest punch diameters, and become even more dominant in the  $\Delta$ -PDF patterns from the punch-only methods [Figs. S4(*a*) and S4(*c*)]. The punch-only methods further reveal an alternation between negative and positive correlations at lattice sites as a function of the punch diameter, with the modulation and their magnitude being dependent on the size and shape of the punch function [Figs. S4(*e*) and S4(*f*)]. Notably, in  $\text{CBr}_4$ , lattice-site correlations will always correspond to same-atom to same-atom correlations, and thus should only result in positive correlations. Negative correlations would suggest there are  $\text{CBr}_4$  molecules with missing constituent atoms, which is not physically reasonable. The formation of such chemical species *in situ* by beam damage, *i.e.* the  $\text{CBr}_3$  radical, is easily observable as a color change from transparent to orange. Such was never observed for any of our neutron scattering experiments, but both the color change and novel pair correlations are observed for synchrotron X-ray diffraction experiments.

Because there is no known plausible physical structural origin for negative correlations on lattice sites in  $\text{CBr}_4$ , and because the observed negative correlations in the calculated  $\Delta$ -PDFs are highly dependent upon the size and shape of the punch functions, it is highly likely that they are artifacts introduced by an incomplete modeling of the diffuse scattering underneath the Bragg peaks. While the punch function does remove the high-frequency features associated with Bragg peaks, the incomplete reconstruction of intensity in the punch regions of reciprocal space also introduces a regular pattern of negative scattering distributed in the exact positions

of the calculated Bragg peaks. This is most apparent for the punch-only methods, for which the discontinuities of the punched voids create new high-frequency features resulting in Gibbs phenomena artifacts in the Fourier analysis. The initial WPC-fill methods with the *SciPy* convolution (Kobas *et al.*, 2005*a,b*) do not sufficiently compensate for the zero intensity of the punched pixels, leaving a regular array of holes throughout the structure, even in regions where there may have been no significant Bragg scattering. The WPC-fill with the *Astropy* convolution and the punch—HC-fill methods better compensate for the zero intensity of the punched voids, although when applied with a fixed lattice-predetermined punch, isotropic Gaussian spheres are regularly placed throughout the reciprocal lattice, constituting a significant contributor to the lattice site artifacts in the  $\Delta$ -PDF. As apparent in Fig. 5(*e*), the HC-fill, particularly for the larger punch diameters, still underfills the diffuse scattering in the Bragg-subtracted void, *i.e.* less than or equivalent to the median of the surrounding diffuse scattering. If too small a punch diameter is used with the HC-fill method, minimizing the underfill artifacts, new artifacts are introduced, as previously described for Fig. S3.

Both the fixed-punch and incomplete-fill methods thus appear to be origins of lattice-site artifacts in  $\Delta$ -PDFs. Fourier analysis of just a set of reciprocal-lattice-site distributed punch reconstructions, whether abrupt voids from the punch-only methods or incompletely filled regions by other methods, would yield positive lattice-site correlations. This is probably the origin of the large  $r$  positive lattice-site correlations most visible in the fixed-punch-only  $\Delta$ -PDF in Figs. S4(*e*) and S4(*f*). However, these punch reconstructions are essentially a virtual element (one with a negative scattering length when under-filled) that is introduced into the system. As such, lattice correlations between real atoms and the virtual element result in a modulated pattern of negative and positive correlations at the lattice sites in the  $\Delta$ -PDFs.

These examples demonstrate that incomplete back-filling of diffuse intensity into the voids resulting from Bragg subtraction creates severe artifacts in the  $\Delta$ -PDF. By contrast, incomplete subtraction of Bragg intensity (or over-filling subtracted voids) only slightly intensifies the already existing real positive lattice correlations in the  $\Delta$ -PDF, while minimal artifacts are introduced. Because of this, we find that the  $\Delta$ -PDF analysis is relatively insensitive to the nature of the fill function, provided that: (i) no sharp discontinuities are introduced that will be manifest as Fourier ripples, (ii) any reconstruction fill of the diffuse scattering under the Bragg scattering over- as opposed to under-estimates the intensity of the diffuse scattering, and (iii) none of the diffuse scattering data are modified other than immediately underneath the outlier-identified Bragg data. Specifically, we found that reconstructing the outlier-identified Bragg voids with the computationally simple (median + 2.2 MAD), or using the computationally more complex parabolic partial differential heat equation, yielded equivalent  $\Delta$ -PDF functions, albeit the former requires three orders of magnitude less computational time. Similarly, we expect the punch—HC-fill method could

also provide an appropriate level of fill were the size of the punch and Gaussian kernel scaled to the size of the punched Bragg peak, and if the punch and reconstruction were only applied to regions with actual Bragg scattering (*e.g.* identified as signal outliers) rather than being applied equivalently at all reciprocal-lattice sites where Bragg intensity may not be experimentally observed.

## 5. Summary

It has long been established that, while Bragg scattering describes a crystalline material's ideal lattice structure, the real structure, resulting from various perturbations to that ideal lattice, gives rise to diffuse scattering. Using model systems of 1D and 2D lattices, we have shown that, though much less intense than Bragg scattering, high-frequency jitter in diffuse scattering data contains critical information for resolving the actual structure. These data challenge the common perception that diffuse scattering is only contained in the low-frequency component of the scattering pattern, and further indicate that low-pass filters or other smoothing functions should not be applied to diffuse scattering data. For the best understanding of diffuse scattering, it is important to employ the highest detector resolution possible.

Though the distinction between Bragg and diffuse scattering is largely defined by some arbitrary intensity threshold, to understand the real-structure deviation from an ideal lattice it is useful to separate the Bragg and diffuse scattering, so that the latter can be evaluated independently. It is further demonstrated that the voids created by subtracting the Bragg scattering must be reconstructed such that no sharp discontinuities are introduced, and the reconstruction must not underfill the void so as to avoid introduction of processing artifacts upon calculation of the 3D  $\Delta$ -PDF. To accomplish this, the *KAREN* algorithm was developed to identify Bragg diffraction as signal outliers which can be removed from the overall scattering data and then replaced by a statistically valid fill value. Importantly, the *KAREN* algorithm is not dependent upon prior knowledge of a system's unit cell. Thus, this method will be invaluable for evaluating complex systems such as modulated structures and/or quasicrystals where prior knowledge of the structure is not easily obtained by experiment. The *KAREN* method for uniquely separating the diffuse from the total scattering is here applied to resolve the complex ordered diffuse scattering exhibited by the plastic crystalline phase of  $\text{CBr}_4$ . The 3D  $\Delta$ -PDF clearly demonstrates that the plastic crystalline phase is not a rotor phase. Rather, the  $\text{CBr}_4$  molecules are disordered about 12 orientations, with the C–Br bonds oriented along the [110] lattice vectors.

## Acknowledgements

This research used resources at the Spallation Neutron Source, a DOE Office of Science User Facility operated by the Oak Ridge National Laboratory. Images of the diffuse scattering and 3D PDFs were created using *SciPy*, *NumPy* and *Matplotlib*.

## Funding information

The following funding is acknowledged: National Science Foundation (award No. 1709370 to James Martin); Oak Ridge National Laboratory (grant No. 4200000570 to Ross Whitfield, James Martin, Christina Hoffmann, Feng Ye).

## References

- Arnold, O., Bilheux, J. C., Borreguero, J. M., Buts, A., Campbell, S. I., Chapon, L., Doucet, M., Draper, N., Ferraz Leal, R., Gigg, M. A., Lynch, V. E., Markvardsen, A., Mikkelsen, D. J., Mikkelsen, R. L., Miller, R., Palmen, K., Parker, P., Passos, G., Perring, T. G., Peterson, P. F., Ren, S., Reuter, M. A., Savici, A. T., Taylor, J. W., Taylor, R. J., Tolchenov, R., Zhou, W. & Zikovsky, J. (2014). *Nucl. Instrum. Methods Phys. Res. A*, **764**, 156–166.
- Bracewell, R. N. (1990). *Science*, **248**, 697–704.
- Bragg, W. L. (1913). *Proc. Cambridge Philos. Soc.* **17**, 43–57.
- Coulon, G. & Descamps, M. (1980). *J. Phys. C Solid State Phys.* **13**, 2847–2846.
- Dill, E. D. (2013). *Determining Melt-Crystallization Mechanisms and Structures of Disordered Crystalline Solids*. PhD thesis. North Carolina State University, Raleigh, North Carolina, USA.
- Egami, T. & Billinge, S. (2012). *Underneath the Bragg Peaks. Structural Analysis of Complex Materials*, Vol. 16. Oxford: Pergamon.
- Folmer, J. C. W., Withers, R. L., Welberry, T. R. & Martin, J. D. (2008). *Phys. Rev. B*, **77**, 144205.
- Friedrich, W., Knipping, P. & Laue, M. (1913). *Ann. Phys.* **346**, 971–988.
- Goossens, D. J., Welberry, T. R., Heerdegen, A. P. & Edwards, A. J. (2005). *Z. Kristallogr.* **220**, 1052–1058.
- Harburn, G., Taylor, C. A. & Welberry, T. R. (1975). *Atlas of Optical Transforms*. London: Bell & Hyman.
- Juhás, P., Davis, T., Farrow, C. L. & Billinge, S. J. L. (2013). *J. Appl. Cryst.* **46**, 560–566.
- Kobas, M., Weber, T. & Steurer, W. (2005a). *Phys. Rev. B*, **71**, 224205.
- Kobas, M., Weber, T. & Steurer, W. (2005b). *Phys. Rev. B*, **71**, 224206.
- Krogstad, M. J., Gehring, P. M., Rosenkranz, S., Osborn, R., Ye, F., Liu, Y., Ruff, J. P. C. & Chen, W. (2018). *DeltaPDF3D-v1*. <https://docs.mantidproject.org/nightly/algorithms/DeltaPDF3D-v1.html>.
- Krogstad, M. J., Rosenkranz, S., Wozniak, J. M., Jennings, G., Ru, J. P. C., Vaughney, J. T. & Osborn, R. (2019). arXiv:1902.03318v1.
- More, M., Lefebvre, J., Hennion, B., Powell, B. M. & Zeyen, C. M. E. (1980). *J. Phys. C Solid State Phys.* **13**, 2833–2846.
- Pearson, R. K., Neuvo, Y., Astola, J. & Gabbouj, M. (2016). *EURASIP J. Adv. Signal Process.* **2016**, 87.
- Price-Whelan, A. M., Sipőcz, B. M., Günther, H. M., Lim, P. L., Crawford, S. M., Conseil, S., Shupe, D. L., Craig, M. W., Dencheva, N., Ginsburg, A., VanderPlas, J. T., Bradley, L. D., Pérez-Suárez, D., de Val-Borro, M., Aldcroft, T. L., Cruz, K. L., Robitaille, T. P., Tollerud, E. J., Ardelean, C., Babej, T., Bachetti, M., Bakanov, A. V., Bamford, S. P., Barentsen, G., Barmby, P., Baumbach, A., Berry, K. L., Biscani, F., Boquien, M., Bostroem, K. A., Bouma, L. G., Brammer, G. B., Bray, E. M., Breytenbach, H., Buddelmeijer, H., Burke, D. J., Calderone, G., Cano Rodríguez, J. L., Cara, M., Cardoso, J. V. M., Cheedella, S., Copin, Y., Crichton, D., DÁvella, D., Deil, C., Depagne, É., Dietrich, J. P., Donath, A., Droettboom, M., Earl, N., Erben, T., Fabbro, S., Ferreira, L. A., Finethy, T., Fox, R. T., Garrison, L. H., Gibbons, S. L. J., Goldstein, D. A., Gommers, R., Greco, J. P., Greenfield, P., Groener, A. M., Grollier, F., Hagen, A., Hirst, P., Homeier, D., Horton, A. J., Hosseinzadeh, G., Hu, L., Hunkeler, J. S., Ivezic, Ž., Jain, A., Jenness, T., Kanarek, G., Kendrew, S., Kern, N. S., Kerzendorf, W. E., Khvalko, A., King, J., Kirkby, D., Kulkarni, A. M., Kumar, A., Lee, A., Lenz, D., Littlefair, S. P., Ma, Z., Macleod, D. M., Mastropietro, M., McCully, C.,

- 1141 Montagnac, S., Morris, B. M., Mueller, M., Mumford, S. J., Muna,  
1142 D., Murphy, N. A., Nelson, S., Nguyen, G. H., Ninan, J. P., Nöthe,  
1143 M., Ogaz, S., Oh, S., Parejko, J. K., Parley, N., Pascual, S., Patil, R.,  
1144 Patil, A. A., Plunkett, A. L., Prochaska, J. X., Rastogi, T., Reddy  
1145 Janga, V., Sabater, J., Sakurikar, P., Seifert, M., Sherbert, L. E.,  
1146 Sherwood-Taylor, H., Shih, A. Y., Sick, J., Silbiger, M. T.,  
1147 Singanamalla, S., Singer, L. P., Sladen, P. H., Sooley, K. A.,  
1148 Sornarajah, S., Streicher, O., Teuben, P., Thomas, S. W., Tremblay,  
1149 G. R., Turner, J. E. H., Terrón, V., van Kerckwijk, M. H., de la Vega,  
1150 A., Watkins, L. L., Weaver, B. A., Whitmore, J. B., Woillez, J. &  
1151 Zabalza, V. (2018). arXiv:1801.02634v2.  
1152 Roth, N. & Iversen, B. B. (2019). *Acta Cryst.* **A75**, 465–473.  
1153 Rousseeuw, P. J. & Croux, C. (1993). *J. Am. Stat. Assoc.* **88**, 1273–1283.  
1154 Sangiorgio, B., Bozin, E. S., Malliakas, C. D., Fechner, M., Simonov,  
1155 A., Kanatzidis, M. G., Billinge, S. J. L., Spaldin, N. A. & Weber, T.  
1156 (2018). *Phys. Rev. Mater.* **2**, 085402.  
1157  
1158  
1159  
1160  
1161  
1162  
1163  
1164  
1165  
1166  
1167  
1168  
1169  
1170  
1171  
1172  
1173  
1174  
1175  
1176  
1177  
1178  
1179  
1180  
1181  
1182  
1183  
1184  
1185  
1186  
1187  
1188  
1189  
1190  
1191  
1192  
1193  
1194  
1195  
1196  
1197
- Schönlieb, C.-B. (2012). *Applying Modern PDE Techniques to Digital  
Image Restoration*. [https://www.mathworks.com/company/  
newsletters/articles/applying-modern-pde-techniques-to-digital-  
image-restoration.html](https://www.mathworks.com/company/newsletters/articles/applying-modern-pde-techniques-to-digital-image-restoration.html).  
Temleitner, L. & Pusztai, L. (2010). *Phys. Rev. B*, **81**, 134101.  
Timmermans, J. (1961). *J. Phys. Chem. Solids*, **18**, 1–8. **[Reference not  
cited - may it be removed?]**  
Weber, T. (2014). *Chimia*, **68**, 60–65.  
Weber, T., Deloudi, S., Kobas, M., Yokoyama, Y., Inoue, A. & Steurer,  
W. (2008). *J. Appl. Cryst.* **41**, 669–674.  
Weber, T. & Simonov, A. (2012). *Z. Kristallogr.* **227**, 238–247.  
Welberry, T. R. & Weber, T. (2015). *Crystallogr. Rev.* **22**, 2–78.  
Wozniak, J. M., Luo, H., Chmaissem, O., Ye, Z.-G. & Phelan, D.  
(2018). *Nat. Mater.* **17**, 718–724. **[Reference not cited - may it be  
removed?]**  
Ye, F., Liu, Y., Whitfield, R., Osborn, R. & Rosenkranz, S. (2018). *J.  
Appl. Cryst.* **51**, 315–322.
- 1198  
1199  
1200  
1201  
1202  
1203  
1204  
1205  
1206  
1207  
1208  
1209  
1210  
1211  
1212  
1213  
1214  
1215  
1216  
1217  
1218  
1219  
1220  
1221  
1222  
1223  
1224  
1225  
1226  
1227  
1228  
1229  
1230  
1231  
1232  
1233  
1234  
1235  
1236  
1237  
1238  
1239  
1240  
1241  
1242  
1243  
1244  
1245  
1246  
1247  
1248  
1249  
1250  
1251  
1252  
1253  
1254